



Article

Diffusion Height and Order of Sulfur Dioxide and Bromine Monoxide Plumes from the Hunga Tonga–Hunga Ha’apai Volcanic Eruption

Qidi Li ^{1,2,†}, Yuanyuan Qian ^{1,2,†}, Yuhan Luo ^{1,*} , Le Cao ³, Haijin Zhou ¹, Taiping Yang ¹ , Fuqi Si ¹ and Wenqing Liu ¹

¹ Key Laboratory of Environmental Optics and Technology, Anhui Institute of Optics and Fine Mechanics, Hefei Institutes of Physical Science, Chinese Academy of Sciences, Hefei 230031, China

² University of Science and Technology of China, Hefei 230026, China

³ Key Laboratory for Aerosol-Cloud-Precipitation of China Meteorological Administration, Nanjing University of Information Science and Technology, Nanjing 210044, China

* Correspondence: yhluo@aiofm.ac.cn

† These authors contributed equally to this work.

Abstract: A violent volcanic eruption attracting considerable attention occurred on 15 January 2022 near the South Pacific island nation of Tonga. To investigate its environmental impact, we retrieved the sulfur dioxide (SO₂) and bromine monoxide (BrO) vertical column densities of environmental trace gas monitoring instrument 2 (EMI-2) based on the differential optical absorption spectroscopy algorithm. The results showed westward and southeastward transport of principal parts of SO₂ and BrO plumes, respectively, from the Hunga Tonga–Hunga Ha’apai (HTHH) eruption. On 15 January, most of the released SO₂ entered the stratosphere (above 20 km) directly and spread rapidly westward (approximately 30 m/s). In contrast, the principal portion of the BrO spread southeastward slowly (approximately 10 m/s) within the 8–15 km altitude layer on 16 January. Our research results also suggest that during the HTHH eruption, BrO was released from the magmatic melt later than SO₂. The total SO₂ emissions from this eruption were approximately 0.24 Tg. The majority of SO₂ and BrO plumes were transported within the Southern Hemisphere. This study is an important extension to the empirical database of volcanological and magmatic degassing research.

Keywords: volcanic emissions; submarine eruptions; DOAS; EMI-2; sulfur dioxide plumes; bromine monoxide plumes



Citation: Li, Q.; Qian, Y.; Luo, Y.; Cao, L.; Zhou, H.; Yang, T.; Si, F.; Liu, W. Diffusion Height and Order of Sulfur Dioxide and Bromine Monoxide Plumes from the Hunga Tonga–Hunga Ha’apai Volcanic Eruption. *Remote Sens.* **2023**, *15*, 1534. <https://doi.org/10.3390/rs15061534>

Academic Editor: Hanlim Lee

Received: 5 February 2023

Revised: 27 February 2023

Accepted: 9 March 2023

Published: 10 March 2023



Copyright: © 2023 by the authors. Licensee MDPI, Basel, Switzerland. This article is an open access article distributed under the terms and conditions of the Creative Commons Attribution (CC BY) license (<https://creativecommons.org/licenses/by/4.0/>).

1. Introduction

Volcanic emissions have a significant influence on the local and global environment and climate. There was a decrease in greenhouse gases in the 2 years following the 1991 eruption of Mount Pinatubo, most likely due to changes in the radiative forcing of the stratospheric circulation [1], leading to a global average surface temperature drop of ~0.2–0.3 °C [2]. Due to sea-ice feedback, cooling can last for up to 16 years after a violent volcanic eruption in the Arctic region [3,4]. Volcanic activity also weakens the monsoon circulation [5–7] and inhibits the global water cycle [8,9]. A recent study suggested a strong link between the 2021 eruption of the La Soufriere volcano and the severe ozone depletion in the Antarctic in that year [10]. The La Soufriere volcanic eruption produced large amounts of stratospheric aerosols, which weakened the wave activity in the Southern Hemisphere stratosphere and reduced the Antarctic stratospheric temperature. They all influence the environment and climate through atmospheric dynamics and atmospheric chemistry. In short, the study of volcanic emissions is essential.

The Hunga Tonga–Hunga Ha’apai (HTHH) is a submarine volcano, and its eruptions destroyed the central part of the Island, and then the plume from the eruption rose into the

atmosphere. The plume from the HTHH volcanic eruption on 15 January 2022 extended over a maximum distance of 57 km vertically [11,12]. The plume is highly perturbing to the stratospheric aerosol and water vapor layers, generates large amounts of radiation, and potentially warms the surface [13,14]. The eruption produced an umbrella cloud similar to that of the 1991 eruption of the Pinatubo volcano and caused significant lightning and tsunamis [15–18], global surface seismic waves [19], and widespread atmospheric waves [17,20]. Investigations of volcanic emission compounds, such as sulfur dioxide (SO₂) and bromine monoxide (BrO), provide essential data on the volcanic eruption processes [21,22].

Relevantly, SO₂ not only affects human health (such as causing respiratory diseases and through acid rain irritating eyes and skin) but also induces climate and environmental change. The oxidation of SO₂ can lead to the formation of aerosols, increased haze, and photochemical smog [23]. The persistence of SO₂ varies from a few days to weeks depending on where it is in the atmosphere. SO₂ generally lasts for only a few days in the troposphere; however, in the lower stratosphere, it can last for several weeks or more [24]. SO₂ vertical column density (VCD) is an essential indicator of air quality and is closely linked to volcanic eruptions. The results of SO₂ VCD and emissions can provide data for air quality monitoring, a database for the traceability of SO₂ pollution and an early warning signal for volcanic eruption activity [25,26].

Bobrowski et al. first identified BrO in volcanic plumes [27] and found that bromine species can deplete ozone in the stratosphere and troposphere [28–30], which has a severe impact on the atmosphere and the climate [31,32]. Consequently, ground-based [33–37] and satellite [38,39] observations have been widely employed in studies on volcanic BrO emission. In addition, plume chemistry models have been developed to analyze the chemical composition of bromine from volcanic eruptions [40,41]. However, the process of bromine degassing is not yet adequately understood because of the paucity of observations and model data [21].

Methods for monitoring volcanic gases include airborne spectrometer measurements, chemical sensor measurements, and satellite observations [42]. As a remote sensing approach, satellite observations are the lowest risk and most labor efficient method as they do not require going in-person inside the active volcano area [22]. Since 1978, satellite remote sensing has contributed essential observations of volcanic eruption gases [43,44]. Carn et al. analyzed the contribution of volcanic SO₂ emission datasets to volcanology using satellite data [45]. Differential optical absorption spectroscopy (DOAS) was introduced by Platt et al. [46] during the 1970s and has been extensively used. It has been widely applied in ground-based [47], airborne, vehicle-borne [48], shipborne, and satellite-based [49] remote sensing. DOAS can measure trace gases such as ozone (O₃), BrO, formaldehyde (HCHO), SO₂, and nitrogen dioxide (NO₂) [50]. On 9 May 2018, China launched the Gaofen-5 (GF-5) satellite, which carried the country's first satellite-based environmental trace-gas monitoring instrument (EMI). The EMI measurements highlighted the validity and reliability of the instrument for retrieval of SO₂ VCD in a volcanic region [51]. EMI-2 is the second-generation model. In this study, we retrieved SO₂ and BrO VCDs from the EMI-2 load based on the DOAS algorithm.

This study analyzed the impact and spread of SO₂ and BrO from the HTHH volcanic eruption. We introduced the HTHH volcano and EMI-2, the retrieval methods and principles of SO₂ and BrO VCDs, and the calculation of SO₂ emissions. Then, we presented the SO₂ and BrO emission results from the HTHH eruption. In addition, we analyzed the wind field data to further investigate the distribution and transport processes of SO₂ and BrO. We also analyzed the sulfur and bromine emissions from HTHH volcano. Finally, we concluded that bromine was released from a magmatic melt later than sulfur during the eruption, and SO₂ and BrO had minor influence on the Northern Hemisphere.

2. Materials and Methods

2.1. The HTHH Volcano

The HTHH volcano (20.536°S, 175.382°W) is a submarine volcano located ~70 km northwest of the capital city of Tonga, Nukualofa. On 13 January 2022 at ~15:00 UTC (14

January 2022 at ~04:00 local time), the first eruption of the HTHH volcano sent a large plume of ashes and gases approximately 20 km above the stratosphere [52]. The HTHH volcano erupted strongly again at ~04:00 UTC (~17:00 local time) on 15 January 2022. The plumes from these eruptions extended over a maximum distance of 57 km, blanketing the surrounding land masses with ash and debris, and triggered severe tsunamis [53]. There was the third and smaller eruption at ~08:00 UTC (~21:00 local time) on 15 January 2022 [11].

2.2. EMI-2

EMI-2 is on board the GF-5 satellite, which was launched on 7 September 2021. EMI-2 is the highest spatial resolution remote sensing payload for atmospheric trace gases in China. EMI-2 utilizes four spectral channels: ultraviolet 1 (240–311 nm), ultraviolet 2 (311–401 nm), visible 1 (401–550 nm), and visible 2 (550–710 nm). In this study, the data for the retrieval of SO₂ were obtained from the ultraviolet-2 channel of EMI-2, with a data dimension of 1473 × 211 × 1072 (time dimension × space dimension × spectral dimension). The spectral resolution of this channel ranges from 0.3 to 0.6 nm, with a nadir spatial resolution of 13 × 24 km². EMI-2 has a field of view of 114°, an altitude of 705 km in orbit, and a transit time of 10:30 am local time. Its descending node is at the equator.

2.3. Calculation of SO₂ and BrO VCDs

As stipulated by the Lambert–Beer law, when natural light penetrates the atmosphere, the solar spectrum changes and the concentration of trace gases in the atmosphere can be measured:

$$\ln \frac{I^*(\lambda)}{I_0(\lambda)} = \sum [\sigma_j^*(\lambda) c_j L] = \sum [\sigma_j^*(\lambda) SCD_j] \quad (1)$$

where $I^*(\lambda)$ denotes the light intensity of the incident light passing through a gas layer of length L , $I_0(\lambda)$ represents the raw luminous intensity of the radiator, $\sigma_j^*(\lambda)$ represents the broadband absorption cross section at wavelength λ of gas j , c_j denotes the average concentration of gas j , $SCD_j = \int c_j L$ represents the slant column density (SCD) of j , and $D = \ln \frac{I^*(\lambda)}{I_0(\lambda)}$ denotes the differential optical density. The SCD of the desired trace gas can be obtained by least-squares fitting using Equation (1).

The SO₂ SCD was retrieved using the QDOAS system [46] in the band between 312 and 326 nm. The absorption cross-sections in this band include SO₂, O₃, NO₂, BrO, HCHO, and ring cross-sections. The ring cross-section was calculated using QDOAS software. Table 1 displays the detailed parameters for the SO₂ spectral fit. Qian et al. provided the SO₂ results from volcanic areas with EMI-2 [54]. Additionally, the SO₂ results were consistent with those from TROPOMI and they are both reliable.

Table 1. Detailed parameters for SO₂ spectral fits.

Parameter	References
SO ₂	298 K [55]
O ₃	223 K, 243 K [56]
NO ₂	220 K, 298 K [57]
BrO	223 K [58]
HCHO	298 K [59]
Ring	Calculated using QDOAS
Fitting Interval	312–326 nm
Polynomial	5

Additionally, we used a QDOAS system to retrieve the BrO VCD. Spectral fits of BrO were conducted in the 330–360 nm wavelength range, and the reference spectrum was the solar spectrum measured by EMI-2. The BrO, O₃, NO₂, O₄, and ring cross-sections were analyzed in the spectral fits. Table 2 lists the detailed parameters of the BrO spectral fits.

Figure 1 shows the spectral fits from the 50th dimension of a track (track number: 211027) on 16 January 2022. The differential SCD (dSCD) for BrO was 4.25×10^{14} molec cm^{-2} , and the root mean square (RMS) for the residuals of the spectral fit was 1.26×10^{-3} .

Table 2. Detailed parameters for BrO spectral fits.

Parameter	References
BrO	223 K [58]
O ₃	223 K, 243 K [56]
NO ₂	298 K [57]
O ₄	293 K [60]
HCHO	298 K [59]
Ring	Calculated using QDOAS
Fitting Interval	330–360 nm
Polynomial	5

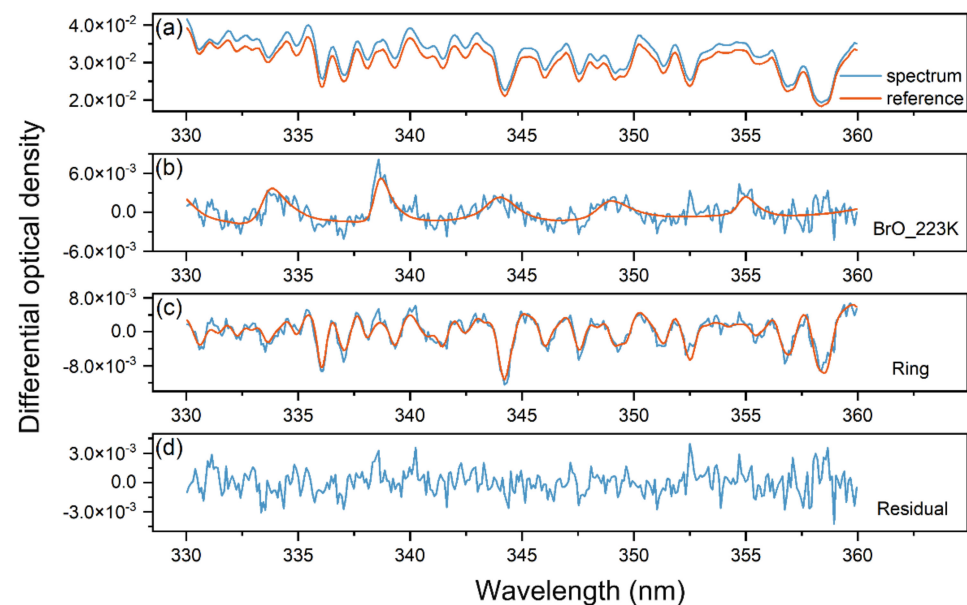


Figure 1. Spectrum fits of BrO on 16 January 2022. (a) measured (blue line) and reference spectrum (orange line); (b) measured (blue line) and fitted (orange line) BrO (223 K) optical density; (c) measured (blue line) and fitted (orange line) Ring optical density; and (d) the remaining residuals of the DOAS.

To obtain a conversion from SCD to VCD, we must consider the air mass factor (AMF), which is obtained by dividing SCD by VCD; that is, $\text{AMF} = \text{SCD}/\text{VCD}$. The lookup tables of the AMFs were obtained using the atmospheric radiative transfer model SCIATRAN. The input parameters for the look-up tables were: solar zenith angle (SZA), relative azimuth angle (RAA), viewing zenith angle (VZA), surface albedo, and cloud pressure. The surface albedo data considered in this research were obtained from a monthly mean climatology dataset based on OMI observations [61] with a spatial resolution of $\text{lat} \times \text{lon} = 0.5^\circ \times 0.5^\circ$. The AMF corresponding to the observed parameters of EMI-2 was obtained using multidimensional linear spatial interpolation, after which the VCD of sulfur dioxide was calculated.

2.4. Calculation of SO₂ Emissions

The emission flux [62] of the SO₂ plume from the volcanic eruption was obtained using the following equation:

$$F = \int_S c \cdot v \cdot n \cdot dS \quad (2)$$

where F denotes the emission flux, c represents the concentration of SO_2 gas mass (g/m^3), and v denotes the wind speed. In addition, n is a unit vector perpendicular to surface S .

The ERA5 dataset from the European Centre for Medium-Range Weather Forecasts website (<https://cds.climate.copernicus.eu/>, accessed on 17 November 2022) provided the wind and temperature fields data. Assuming a relatively stable wind field during the observation period, the emission flux of the SO_2 plume after it has moved in response to the wind field was obtained as follows:

$$F = \left(\sum_i V_{CD,i} \cdot l_i \right) \cdot v \cdot \cos(\theta) \quad (3)$$

where l_i denotes the horizontal length of the i th pixel, and θ indicates the angle in the wind field direction along the longitudinal direction. For an SO_2 plume at a distance of d from the eruption point, the above equation can be rewritten as:

$$F = \left(\sum_i V_{CD,i} \cdot l_i \right) \cdot v \cdot \cos(\theta) \cdot \exp\left(-\frac{d}{\tau}\right) \quad (4)$$

where τ denotes the duration of the SO_2 plume from the volcanic eruption. The emission of the SO_2 plume was obtained as follows:

$$M = F \cdot t \quad (5)$$

where M denotes the emission, and t represents the duration of the eruption.

3. Results

3.1. Spread of SO_2 and BrO

Figure 2 illustrates the different distributions and transports of SO_2 and BrO plumes from this eruption; panels (a), (c), (e), (g), (i), and (k) show the SO_2 VCD results from the retrieval of EMI-2 data for 14–19 January 2022.

On 14 January 2022, EMI-2 observations showed that SO_2 was mainly located in the 20°S – 25°S , 170°W – 180°W region, with a maximum value > 10 DU. On 15 January, the SO_2 mostly spread to the northwest, mainly located in the 15°S – 25°S , 170°W – 180°W , and 170°E – 180°E region. The area with the highest SO_2 concentration inside the plume was located along several latitudes and longitudes around (23°S , 175°E), whereas the area with the lowest SO_2 concentration was between 170°W and 180°W . On 16 January, the principal part of SO_2 continued to spread westward and partially reached near 160°E . On 17 January, the SO_2 had reached near 140°E in northeastern Australia. The principal portion of SO_2 was located over the sea to the northeast of Australia, and the overall SO_2 above the ocean continued to spread northwestward. On 18 January, the principal part of SO_2 reached near 130°E , with a northwest-southeast distribution over the sea, while on 19 January, it reached approximately 110°E , having already crossed Australia. Overall, the spatial distribution of SO_2 VCDs from the EMI-2 retrieval for 14–19 January 2022 showed a westward transport of the principal part of the SO_2 plume from this eruption.

Panels (b), (d), (f), (h), (j), and (l) of Figure 2 show the distribution and transport of the BrO plume from this eruption for 14–19 January 2022. On 14–15 January, the BrO plume of HTHH submarine volcano was not significantly detected, possibly because there was a thimbleful of BrO emissions. On 16 January, the EMI-2 observations evidently indicated the two regions with BrO plume. Essentially, BrO from the HTHH volcanic eruptions was detected later than SO_2 . The principal part of BrO was in the (17°S – 30°S , 170°W – 180°W) region, with maximum value above 1.5×10^{14} molec cm^{-2} . The smaller part of BrO spread westwards into the region of (17°S – 25°S , 170°E – 178°E). On 17 January, the principal part of BrO spread to the southeast and reached near 40°S . In contrast, the smaller part of BrO continued to spread westwards and reached near 150°E . On 18 January, the principal part of BrO spread southeastwards to around 45°S , 160°W . The other part of BrO reached near

130°E in northeastern Australia. On 19 January, the principal part of BrO continued to spread eastwards and reached near 150°W, while the smaller part reached near 120°E in northwestern Australia. The BrO plume was gradually diluted, and the concentration range was mainly in 5.0×10^{13} – 10.0×10^{13} molec cm^{-2} .

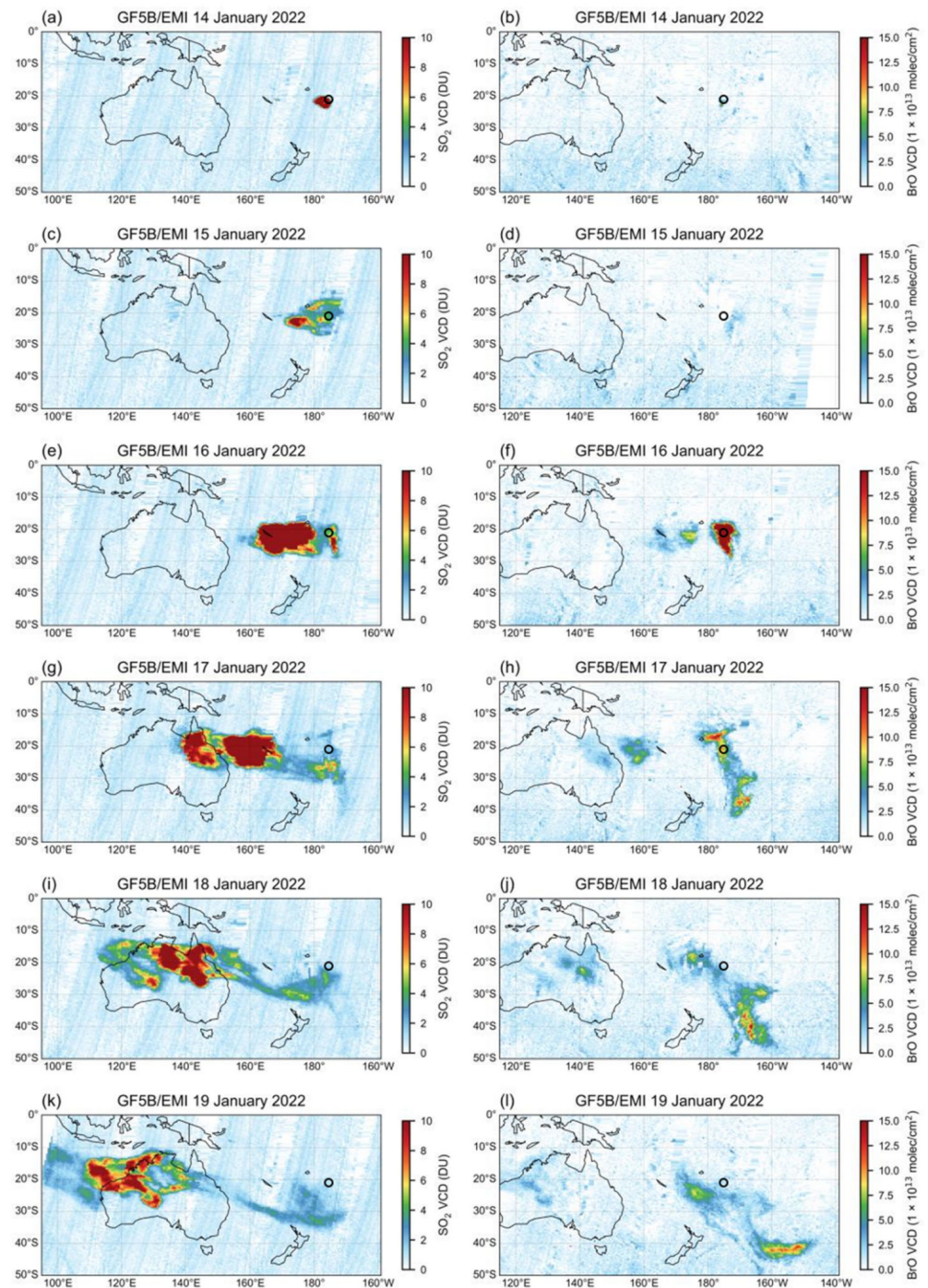


Figure 2. Monitored SO_2 and BrO VCDs and location (black circle) of the HTHH submarine volcano. The x label is the longitude and the y label is the latitude. (a) SO_2 VCD on 14 January 2022; (b) BrO VCD on 14 January 2022; (c) SO_2 VCD on 15 January 2022; (d) BrO VCD on 15 January 2022; (e) SO_2 VCD on 16 January 2022; (f) BrO VCD on 16 January 2022; (g) SO_2 VCD on 17 January 2022; (h) BrO VCD on 17 January 2022; (i) SO_2 VCD on 18 January 2022; (j) BrO VCD on 18 January 2022; (k) SO_2 VCD on 19 January 2022; (l) BrO VCD on 19 January 2022.

3.2. Relation of the Spread of SO₂ and BrO to Wind Fields

To further investigate the distribution and transport processes of SO₂ and BrO released from the HTHH submarine volcano eruptions, we analyzed the average vertical distribution of wind and temperature fields at an altitude of 0–32 km in the 20–25°S latitude zone on 14–19 January 2022. The results are presented in Figure 3. Appendix A shows the average vertical distribution of wind and temperature fields in the 15–20°S (Figure A1), 25–30°S (Figure A2), 30–35°S (Figure A3), and 35–40°S (Figure A4) latitude zones. The ERA5 dataset provided the wind and temperature field data used in this study.

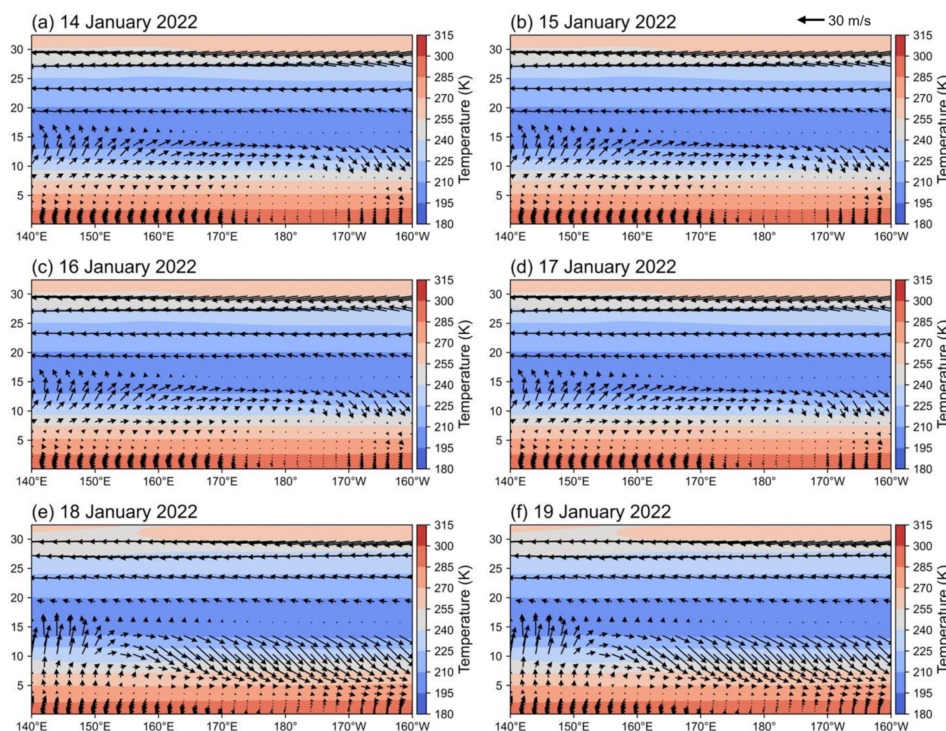


Figure 3. Average vertical wind field and temperature field at the altitude of 0–32 km in the 20–25°S latitude zone. The x label is the longitude and the y label is the latitude. (a) Vertical wind and temperature field on 14 January 2022; (b) vertical wind and temperature field on 15 January 2022; (c) vertical wind and temperature field on 16 January 2022; (d) vertical wind and temperature field on 17 January 2022; (e) vertical wind and temperature field on 18 January 2022; (f) vertical wind and temperature field on 19 January 2022.

As illustrated in Figure 3, on 15 January 2022, temperatures ranged from ~195–210 K at an altitude of 15–20 km, and wind speeds were low in the volcanic region. Above an altitude of 20 km, the wind in the atmosphere was predominantly easterly. In contrast, in the 8–15 km altitude range, the wind was predominantly westerly in the volcanic region. As wind speeds were very low below 8 km in the volcanic region, the diffusion of gases from the HTHH volcanic eruptions at this altitude was weak and, thus, was not considered in this study. In the volcanic region, SO₂ in the stratosphere gradually spread to the west. However, SO₂ in the troposphere spread to the southeast. Existing studies [44,63,64], of the HTHH eruption have identified a westward movement of the SO₂ plume. However, our study demonstrates that the SO₂ plume was moving southeastward in the troposphere.

The 15–20 km altitude layer showed different transmission dynamics. On 16 January, the relatively much higher concentration is caused by the upward motion and stronger convergence, which can bring more SO₂ and BrO into the upper layer. By contrast, there is downward motion east of 180°, which inhibits the vertical transport of SO₂ and BrO and results in a lot of deposition into the surface. Most of the SO₂ from the HTHH volcano eruptions spread significantly westward due to easterly winds and reached ~160°E. Thus,

the principal part of the SO₂ was above an altitude of 20 km. As wind speeds in the troposphere were significantly lower than those in the stratosphere, a small proportion of SO₂ at an altitude of 8–15 km spread slowly eastward and reached ~170°W. A small proportion of BrO was pushed above an altitude of 20 km and spread westward near 170°E. However, the principal part of the BrO was in the 8–15 km altitude range and spread southeastward to near 30°S, 170°W. On 17 January, stratospheric SO₂ continued to spread westward and reached close to 140°E. However, tropospheric SO₂ continued to spread southeastward and reached near 30°S. The tropospheric BrO spread consistently to the southeast, while the stratospheric BrO spread consistently to the west. On 18 January, the principal part of BrO spread southeastwards to around 160°W, and a small amount of SO₂ reached near 110°E. On 19 January, a large amount of SO₂ reached near 110°E, and the principal part of BrO continued to spread eastwards and reached near 150°W. Figure 4 shows the diagram of the three volcanic eruptions. We presume that SO₂ and BrO were erupted to different altitudes. This may be due to SO₂ and BrO being erupted with different intensities. As known from the references and satellite observations, a small amount of SO₂ and a thimbleful of BrO was erupted in the first eruption at ~15:00 UTC on 13 January (~04:00 local time on 14 January) 2022. Then, large amounts of SO₂ were violently erupted at ~04:00 UTC (~17:00 local time) on 15 January 2022, entering the stratosphere (up to 57 km) directly. Follow the westward wind above 20 km altitude, most SO₂ spread westward. However, the bulk of the BrO transmitted in the southeastward direction, which means there was little BrO during the second eruption. Thereby, most of the BrO was erupted in the third and weaker eruption at ~08:00 UTC (~21:00 local time) on 15 January 2022, where the eruption height was below 20 km. The southeastward wind field under 20 km provided reasonable explanation for the transmission of the BrO plume. However, the process of bromine degassing is not yet adequately understood.

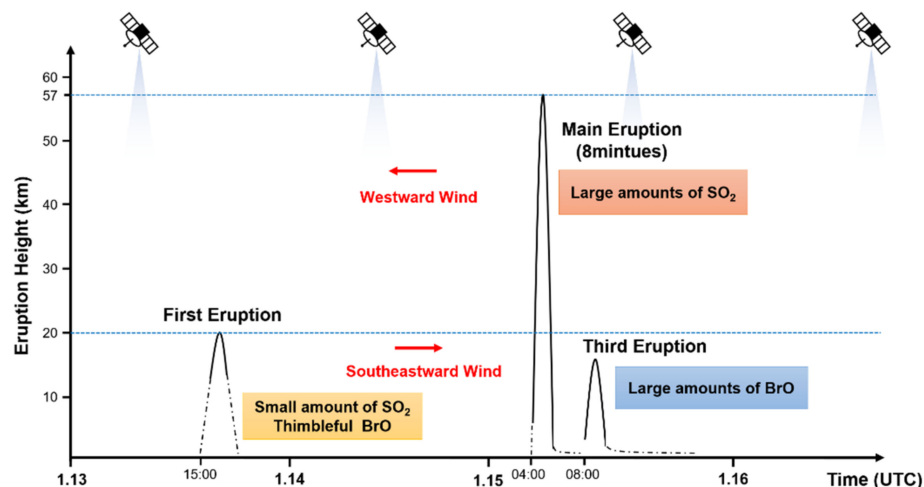


Figure 4. Diagram of the three volcanic eruptions.

4. Discussion

The violent volcanic eruption that occurred on 15 January 2022 near Tonga attracted considerable research attention, especially given that SO₂ and BrO levels and distribution patterns in volcanic emissions revealed essential information on the volcanic eruption processes. Here, we took advantage of the DOAS algorithm combined with EMI-2 data to investigate the impact and spread of SO₂ and BrO plumes from the January 15 volcanic eruption.

Notably, chlorine emissions have also been proposed as a crucial indicator for predicting volcanic eruptions [65–69]. Molten fluids of halogens (especially chlorine) and sulfur have also attracted a great deal of attention [70,71]. Chlorine had a lower melt-fluid partitioning rate than sulfur, concluding that chlorine was usually released from magma later than sulfur [72].

In contrast, the process of bromine degassing is inadequately understood; lack of data has stymied a clear consensus on whether bromine is released from the magma earlier than sulfur. BrO is not an important bromine species in magmatic gases, which are rapidly formed when the volcano plume enters the atmosphere. Due to the autocatalytic bromine explosion mechanism [73], the BrO concentration can be expected to increase quickly under sunlight through photolysis [74].

Bobrowski and Giuffrida [75] assumed that sulfur was released from magmatic melts after bromine. However, numerous studies have suggested that sulfur is released from magma melts earlier than chlorine. Later, Lübcke et al. [76] observed that volcanic bromine and sulfur emissions were associated with seismic events. They discussed two possibilities: bromine being released first or sulfur being released first, with each being equally plausible. Cadoux et al. [77] observed that the melt-fluid partitioning coefficients for bromine ranged from 3.8 to 20.8. This is comparable to that of chlorine, which has melt-fluid partition coefficients of 0.3–50 [78,79]. These values were both lower than the melt-fluid partition coefficients for sulfur, which ranged from 3 to 236 [80]. Thus, they suggested that bromine was consistent with chlorine and that bromine should be released after sulfur in magmatic melts. [77].

Our observations found that SO₂ was detected on 14 January, whereas most of the BrO was detected on 16 January. The BrO in the volcanic plume could be explained as rapidly produced by the autocatalytic inhomogeneous oxidation of HBr released from the volcanic eruption [32]. We concluded that bromine was released later than sulfur, from a magmatic melt during the eruption patterns of the HTHH volcano. Thus, further investigation of bromine could provide useful information for volcanologists.

As different transportation occurred in the 20–30 km and 8–15 km altitude layers, we analyzed average horizontal wind fields at these altitudes for the 14–19 January 2022 period (Figures 5 and 6). The Southern Hemisphere experiences summer during this period, with relatively straight easterly jet streams dominating the stratospheric wind field at low and medium latitudes. Most of the SO₂ released from the HTHH eruption entered the stratosphere directly and spread rapidly westward (approximately 30 m/s) via jet streams on 15 January. In contrast, only a small part of the BrO spread westward in this manner.

As shown in Figure 6, the tropospheric wind field was irregular, and wind speeds were significantly lower than those in the stratosphere. SO₂ in the troposphere spread slowly to the southeast between 14 and 19 January, with a transport interval mainly in the 10–40°S latitude band. Similarly, BrO in the troposphere spread slowly to the southeast because of northwesterly winds between 16 and 19 January, reaching near 40°S, 150°W. The principal portion of the BrO spread southeastward slowly (approximately 10 m/s) within the 8–15 km altitude layer on 16 January. Furthermore, because of the relatively independent wind circulation in the northern and southern hemispheres and the weak trans-equatorial transport, the majority of SO₂ and BrO was transported throughout the Southern Hemisphere.

As the SO₂ plume from this eruption had reached the stratosphere and had a long lifetime, Equation (4) can be replaced by Equation (3) to calculate the SO₂ emission from the HTHH volcanic eruption, where the wind field data are also from the ECMWF reanalysis dataset. The eruption on 15 January lasted 8 min and caused huge volumes of ash to rise rapidly and cover Tonga [81]. Using Equation (5), we estimated that the total SO₂ emissions from the 15 January eruption were ~0.24 Tg. In another study by Carn et al. [63], the initial estimate of the total SO₂ emissions released from this eruption on 15 January 2022 was ~0.4 Tg. However, our results may be lower because of subsequent small-scale eruptions. Compared to the 20 Tg SO₂ released by Mount Pinatubo (Philippines) in 1991 [82] and ~7.5 Tg SO₂ released by El Chichón in 1982 [83], the amount of SO₂ from the HTHH volcano was lower. The HTHH volcano has abundant brine that interacts with magma, unlike the Mount Pinatubo and El Chichón volcanoes. Therefore, a large amount of SO₂ released from the HTHH volcano was probably removed by wet deposition [84,85].

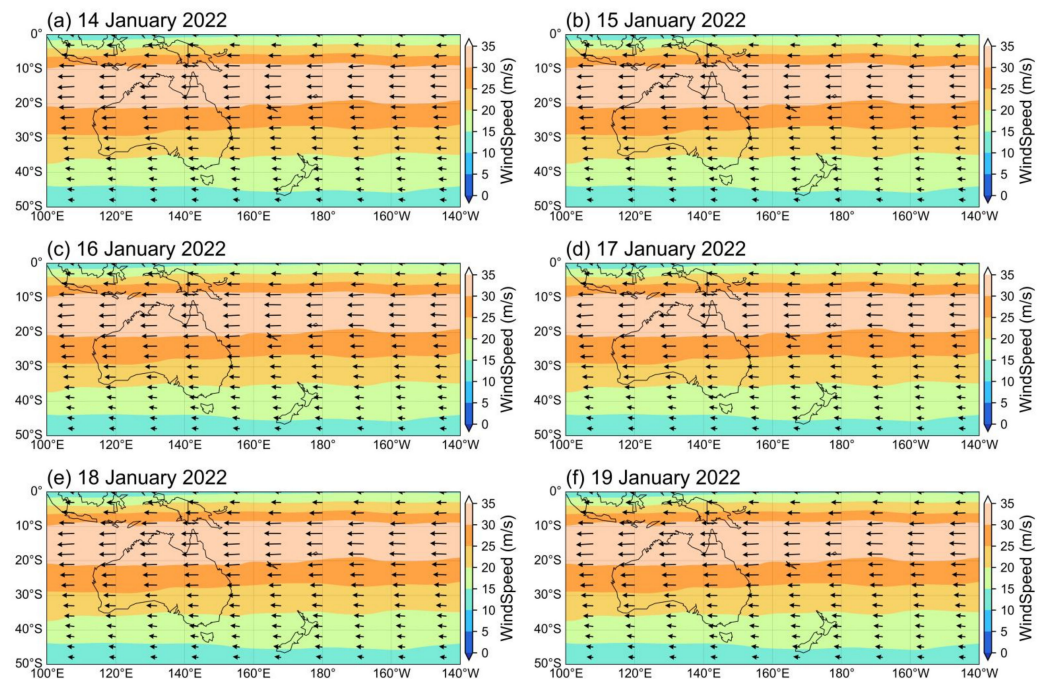


Figure 5. Average horizontal wind field at the altitude of 20–30 km. The x label is the longitude and the y label is the latitude. (a) Horizontal wind field on 14 January 2022; (b) horizontal wind field on 15 January 2022; (c) horizontal wind field on 16 January 2022; (d) horizontal wind field on 17 January 2022; (e) horizontal wind field on 18 January 2022; (f) horizontal wind field on 19 January 2022.

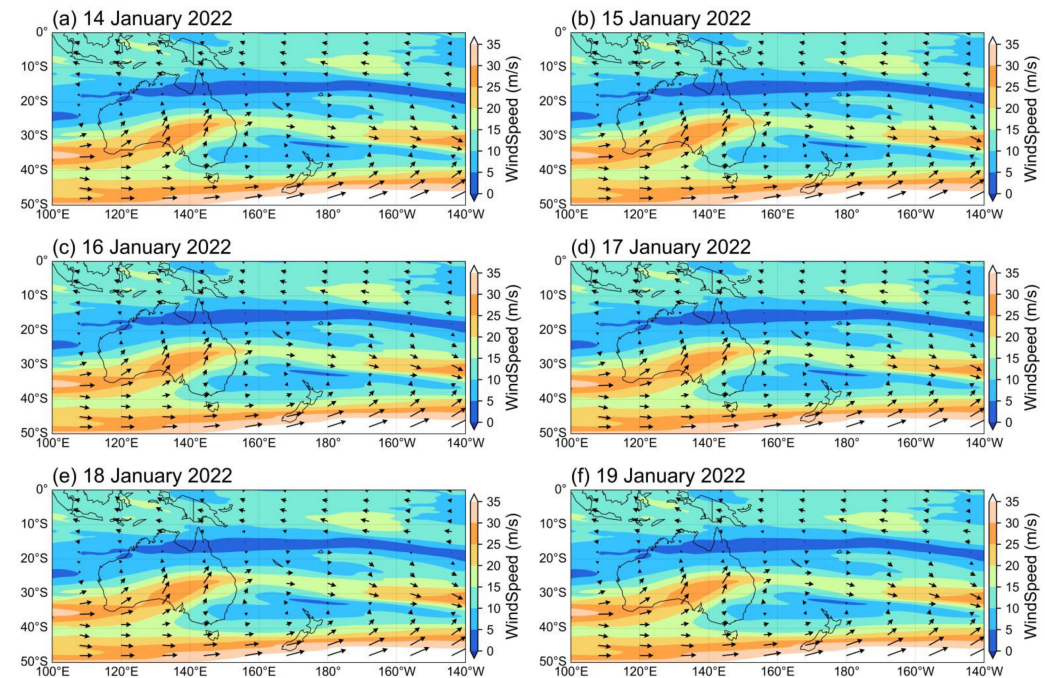


Figure 6. Average horizontal wind field at the altitude of 8–15 km. The x label is the longitude and the y label is the latitude. (a) Horizontal wind field on 14 January 2022; (b) horizontal wind field on 15 January 2022; (c) horizontal wind field on 16 January 2022; (d) horizontal wind field on 17 January 2022; (e) horizontal wind field on 18 January 2022; (f) horizontal wind field on 19 January 2022.

In summary, because of the relatively independent wind circulations of the Northern and Southern Hemispheres as well as the weak trans-equatorial transport, a major portion of SO_2 and BrO was transported within the Southern Hemisphere. Additionally, SO_2

emissions from the HTHH volcano were low, and thus the effects of SO₂ and BrO on the Northern Hemisphere were minor.

5. Conclusions

Using the DOAS algorithm, we successfully retrieved EMI-2 SO₂ VCDs and BrO VCDs for the HTHH volcanic eruption. Overall, the spatial distribution of SO₂ VCDs from the EMI-2 retrieval for 14–19 January 2022 showed westward transportation of the principal part of the SO₂ plume. On 16 January, EMI-2 observations indicated two regions where the BrO plume was apparent. The principal part of BrO spread slowly southeastward, whereas a small part of BrO spread rapidly westward.

Most of the SO₂ released from this eruption entered the stratosphere (above 20 km) directly and spread rapidly westward by jet streams. In contrast, the principal part of BrO was in the 8–15 km altitude layer and spread slowly southeastwards. Additionally, based on our observations, we conclude that bromine was released later than sulfur, from a magmatic melt during this eruption.

The lower SO₂ emission from the January 15 HTHH volcanic eruption, equal to ~0.24 Tg, compared to that of Mount Pinatubo (1991) and El Chichón (1982) eruptions, can be attributed to the fact that the HTHH volcano is submarine type with abundant seawater available for magma interaction. Moreover, a major part of SO₂ and BrO was transported in the Southern Hemisphere. Additionally, the influence of SO₂ and BrO on the Northern Hemisphere was found to be minor. This study is an important extension of an empirical database of volcanological and magmatic degassing research. In the future, integrated analyses based on numerical models and observational data will be necessary to study volcanic activity and its impact on climate change and the ecological environment.

Author Contributions: Methodology, Q.L., Y.Q. and Y.L.; Investigation, Q.L. and Y.Q.; Software, Q.L. and Y.Q.; Formal analysis, Q.L., Y.Q., Y.L. and L.C.; Validation, Y.L., L.C. and F.S.; Visualization, Q.L. and Y.Q.; Writing, Q.L. and Y.L.; Reviewing, Y.L.; Editing, Y.L.; Resource, Y.L., H.Z., F.S. and T.Y.; Funding acquisition, Y.L.; Supervision, Y.L., F.S. and W.L. All authors have read and agreed to the published version of the manuscript.

Funding: This study was financially supported by the National Natural Science Foundation of China (Grant Nos. 41941011 and 41676184) and the Youth Innovation Promotion Association of CAS (Grant No. 2020439).

Data Availability Statement: The data used in this research are available from Yuhan Luo from AIOFM, CAS (yhluo@aiofm.ac.cn).

Acknowledgments: We are thankful to the Ministry of Ecology and Environment Satellite Application Center for Ecology and Environment (SACEE) for providing the EMI-2 level 1 data. We gratefully thank the BIRA for providing the QDOAS software. We also gratefully thank ECMWF for providing the wind-field data.

Conflicts of Interest: The authors declare no conflict of interest.

Appendix A

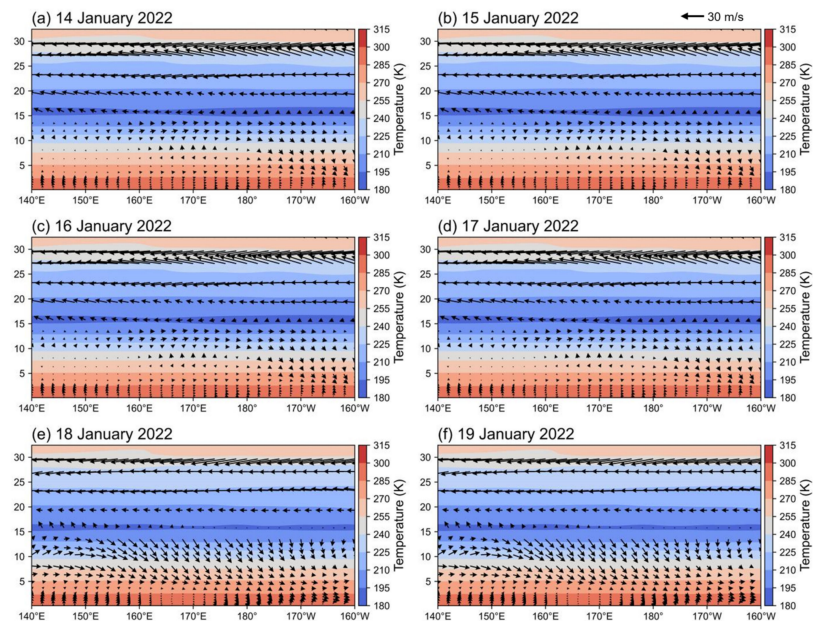


Figure A1. Average vertical wind field and temperature field at the altitude of 0–32 km in the 15–20°S latitude zone. The x label is the longitude and the y label is the latitude. (a) Vertical wind and temperature field on 14 January 2022; (b) vertical wind and temperature field on 15 January 2022; (c) vertical wind and temperature field on 16 January 2022; (d) vertical wind and temperature field on 17 January 2022; (e) vertical wind and temperature field on 18 January 2022; (f) vertical wind and temperature field on 19 January 2022.

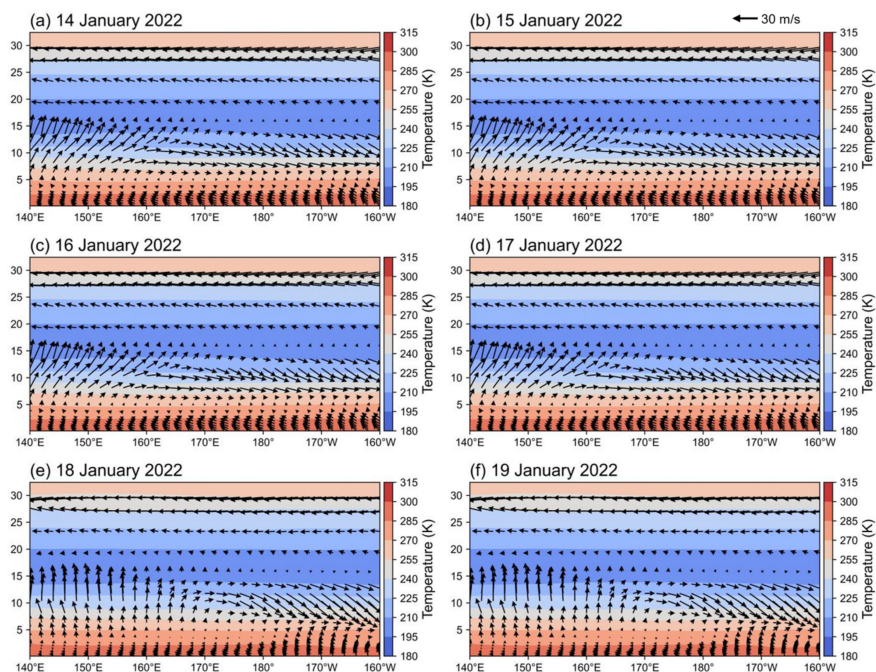


Figure A2. Average vertical wind field and temperature field at the altitude of 0–32 km in the 25–30°S latitude zone. The x label is the longitude and the y label is the latitude. (a) Vertical wind and temperature field on 14 January 2022; (b) vertical wind and temperature field on 15 January 2022; (c) vertical wind and temperature field on 16 January 2022; (d) vertical wind and temperature field on 17 January 2022; (e) vertical wind and temperature field on 18 January 2022; (f) vertical wind and temperature field on 19 January 2022.

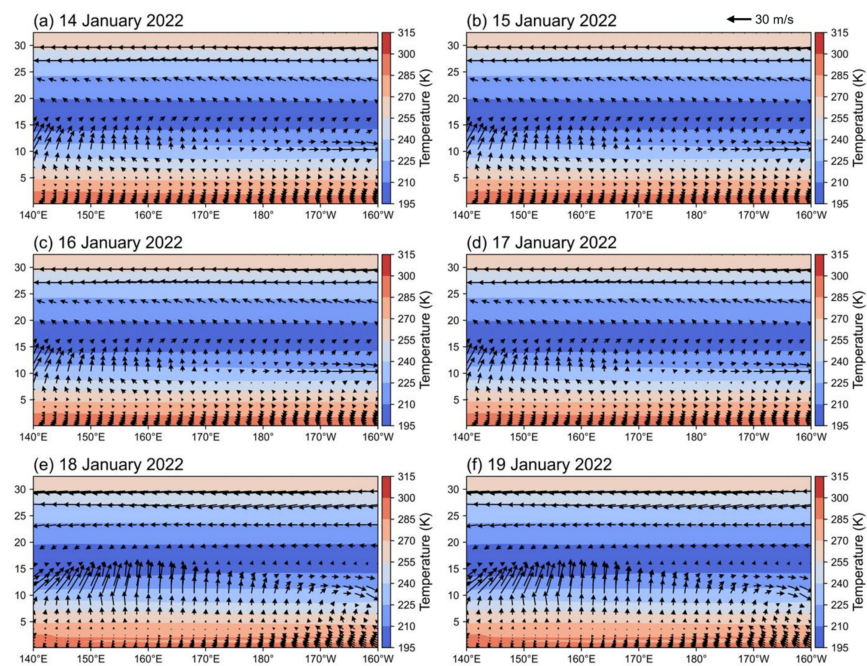


Figure A3. Average vertical wind field and temperature field at the altitude of 0–32 km in the 30–35°S latitude zone. The x label is the longitude and the y label is the latitude. (a) Vertical wind and temperature field on 14 January 2022; (b) vertical wind and temperature field on 15 January 2022; (c) vertical wind and temperature field on 16 January 2022; (d) vertical wind and temperature field on 17 January 2022; (e) vertical wind and temperature field on 18 January 2022; (f) vertical wind and temperature field on 19 January 2022.

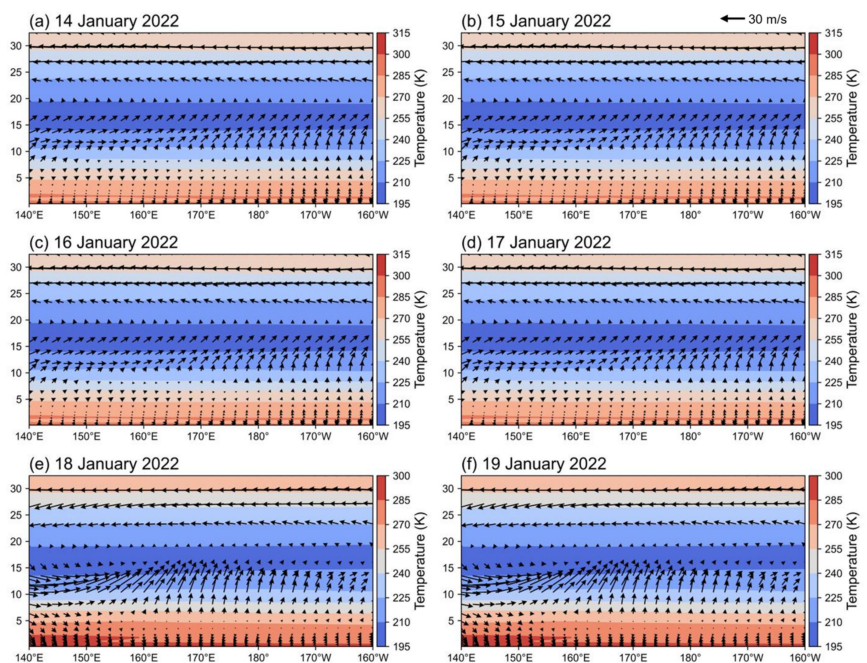


Figure A4. Average vertical wind field and temperature field at the altitude of 0–32 km in the 35–40°S latitude zone. The x label is the longitude and the y label is the latitude. (a) Vertical wind and temperature field on 14 January 2022; (b) vertical wind and temperature field on 15 January 2022; (c) vertical wind and temperature field on 16 January 2022; (d) vertical wind and temperature field on 17 January 2022; (e) vertical wind and temperature field on 18 January 2022; (f) vertical wind and temperature field on 19 January 2022.

References

1. Pitari, G.; Mancini, E. Short-term climatic impact of the 1991 volcanic eruption of Mt. Pinatubo and effects on atmospheric tracers. *Nat. Hazards Earth Syst. Sci.* **2002**, *2*, 91–108. [[CrossRef](#)]
2. Stenchikov, G.; Robock, A.; Ramaswamy, V.; Schwarzkopf, M.D.; Hamilton, K.; Ramachandran, S. Arctic Oscillation response to the 1991 Mount Pinatubo eruption: Effects of volcanic aerosols and ozone depletion. *J. Geophys. Res. Atmos.* **2002**, *107*, ACL 28-1–ACL 28-16. [[CrossRef](#)]
3. Miller, G.H.; Geirsdóttir, Á.; Zhong, Y.; Larsen, D.J.; Otto-Bliesner, B.L.; Holland, M.M.; Bailey, D.A.; Refsnider, K.A.; Lehman, S.J.; Southon, J.R. Abrupt onset of the Little Ice Age triggered by volcanism and sustained by sea-ice/ocean feedbacks. *Geophys. Res. Lett.* **2012**, *39*, L02708. [[CrossRef](#)]
4. Liu, B.; Zhao, C.; Zhu, L.; Liu, J. Seasonal changes in arctic cooling after single mega volcanic eruption. *Front. Earth Sci.* **2021**, *9*, 688250. [[CrossRef](#)]
5. Man, W.; Zhou, T.; Jungclaus, J.H. Simulation of the East Asian summer monsoon during the last millennium with the MPI Earth System Model. *J. Clim.* **2012**, *25*, 7852–7866. [[CrossRef](#)]
6. Man, W.; Zhou, T. Response of the East Asian summer monsoon to large volcanic eruptions during the last millennium. *Chin. Sci. Bull.* **2014**, *59*, 4123–4129. [[CrossRef](#)]
7. Liu, F.; Chai, J.; Wang, B.; Liu, J.; Zhang, X.; Wang, Z. Global monsoon precipitation responses to large volcanic eruptions. *Sci. Rep.* **2016**, *6*, 24331. [[CrossRef](#)]
8. Robock, A. Volcanic eruptions and climate. *Rev. Geophys.* **2000**, *38*, 191–219. [[CrossRef](#)]
9. Timmreck, C. Modeling the climatic effects of large explosive volcanic eruptions. *Wiley Interdiscip. Rev. Clim. Change* **2012**, *3*, 545–564. [[CrossRef](#)]
10. Yook, S.; Thompson, D.W.; Solomon, S. Climate impacts and potential drivers of the unprecedented Antarctic ozone holes of 2020 and 2021. *Geophys. Res. Lett.* **2022**, *49*, e2022GL098064. [[CrossRef](#)]
11. Proud, S.R.; Prata, A.T.; Schmauß, S. The January 2022 eruption of Hunga Tonga-Hunga Ha’apai volcano reached the mesosphere. *Science* **2022**, *378*, 554–557. [[CrossRef](#)]
12. Carr, J.L.; Horváth, Á.; Wu, D.L.; Friberg, M.D. Stereo plume height and motion retrievals for the record-setting Hunga Tonga-Hunga Ha’apai eruption of 15 January 2022. *Geophys. Res. Lett.* **2022**, *49*, e2022GL098131. [[CrossRef](#)]
13. Millán, L.; Santee, M.L.; Lambert, A.; Livesey, N.J.; Werner, F.; Schwartz, M.J.; Pumphrey, H.C.; Manney, G.L.; Wang, Y.; Su, H. The Hunga Tonga-Hunga Ha’apai hydration of the stratosphere. *Geophys. Res. Lett.* **2022**, *49*, e2022GL099381. [[CrossRef](#)]
14. Sellitto, P.; Podglajen, A.; Belhadji, R.; Boichu, M.; Carboni, E.; Cuesta, J.; Duchamp, C.; Kloss, C.; Siddans, R.; Bègue, N. The unexpected radiative impact of the Hunga Tonga eruption of 15th January 2022. *Commun. Earth Environ.* **2022**, *3*, 288. [[CrossRef](#)]
15. Gupta, A.K.; Bennartz, R.; Fauria, K.E.; Mittal, T. Eruption chronology of the December 2021 to January 2022 Hunga Tonga-Hunga Ha’apai eruption sequence. *Commun. Earth Environ.* **2022**, *3*, 314. [[CrossRef](#)]
16. Kubota, T.; Saito, T.; Nishida, K. Global fast-traveling tsunamis driven by atmospheric Lamb waves on the 2022 Tonga eruption. *Science* **2022**, *377*, 91–94. [[CrossRef](#)]
17. Matoza, R.S.; Fee, D.; Assink, J.D.; Iezzi, A.M.; Green, D.N.; Kim, K.; Toney, L.; Lecocq, T.; Krishnamoorthy, S.; Lalande, J.-M. Atmospheric waves and global seismoacoustic observations of the January 2022 Hunga eruption, Tonga. *Science* **2022**, *377*, 95–100. [[CrossRef](#)]
18. Yuen, D.A.; Scruggs, M.A.; Spera, F.J.; Zheng, Y.; Hu, H.; McNutt, S.R.; Thompson, G.; Mandli, K.; Keller, B.R.; Wei, S.S. Under the surface: Pressure-induced planetary-scale waves, volcanic lightning, and gaseous clouds caused by the submarine eruption of Hunga Tonga-Hunga Ha’apai volcano. *Earthq. Res. Adv.* **2022**, *2*, 100134. [[CrossRef](#)]
19. Poli, P.; Shapiro, N.M. Rapid characterization of large volcanic eruptions: Measuring the impulse of the Hunga Tonga Ha’apai explosion from teleseismic waves. *Geophys. Res. Lett.* **2022**, *49*, e2022GL098123. [[CrossRef](#)]
20. Podglajen, A.; le Pichon, A.; Garcia, R.F.; Gèrier, S.; Millet, C.; Bedka, K.; Khlopenkov, K.; Khaykin, S.; Hertzog, A. Stratospheric Balloon Observations of Infrasound Waves From the 15 January 2022 Hunga Eruption, Tonga. *Geophys. Res. Lett.* **2022**, *49*, e2022GL100833. [[CrossRef](#)]
21. Warnach, S.; Bobrowski, N.; Hidalgo, S.; Arellano, S.; Sihler, H.; Dinger, F.; Lübcke, P.; Battaglia, J.; Steele, A.; Galle, B. Variation of the BrO/SO₂ molar ratio in the plume of Tungurahua Volcano between 2007 and 2017 and its relationship to volcanic activity. *Front. Earth Sci.* **2019**, *7*, 132. [[CrossRef](#)]
22. Dinger, F.; Kleinbek, T.; Dörner, S.; Bobrowski, N.; Platt, U.; Wagner, T.; Ibarra, M.; Espinoza, E. SO₂ and BrO emissions of Masaya volcano from 2014 to 2020. *Atmos. Chem. Phys.* **2021**, *21*, 9367–9404. [[CrossRef](#)]
23. Theys, N.; de Smedt, I.; van Gent, J.; Danckaert, T.; Wang, T.; Hendrick, F.; Stavrakou, T.; Bauduin, S.; Clarisse, L.; Li, C. Sulfur dioxide vertical column DOAS retrievals from the Ozone Monitoring Instrument: Global observations and comparison to ground-based and satellite data. *J. Geophys. Res. Atmos.* **2015**, *120*, 2470–2491. [[CrossRef](#)]
24. Khattak, P.; Khokhar, M.F.; Yasmin, N. Spatio-temporal analyses of atmospheric sulfur dioxide column densities over Pakistan by using SCIAMACHY data. *Aerosol Air Qual. Res.* **2014**, *14*, 1883–1896. [[CrossRef](#)]
25. Oppenheimer, C.; Fischer, T.; Scaillet, B. Volcanic degassing: Process and impact. *Treatise Geochem.* **2014**, *4*, 111–179.
26. Hidalgo, S.; Battaglia, J.; Arellano, S.; Sierra, D.; Bernard, B.; Parra, R.; Kelly, P.; Dinger, F.; Barrington, C.; Samaniego, P. Evolution of the 2015 Cotopaxi eruption revealed by combined geochemical and seismic observations. *Geochem. Geophys. Geosyst.* **2018**, *19*, 2087–2108. [[CrossRef](#)]

27. Bobrowski, N.; Hönninger, G.; Galle, B.; Platt, U. Detection of bromine monoxide in a volcanic plume. *Nature* **2003**, *423*, 273–276. [[CrossRef](#)]
28. Finlayson-Pitts, B.; Livingston, F.; Berko, H. Ozone destruction and bromine photochemistry at ground level in the Arctic spring. *Nature* **1990**, *343*, 622–625. [[CrossRef](#)]
29. Prather, M.J.; Watson, R.T. Stratospheric ozone depletion and future levels of atmospheric chlorine and bromine. *Nature* **1990**, *344*, 729–734. [[CrossRef](#)]
30. Lary, D. Gas phase atmospheric bromine photochemistry. *J. Geophys. Res. Atmos.* **1996**, *101*, 1505–1516. [[CrossRef](#)]
31. Platt, U.; Hönninger, G. The role of halogen species in the troposphere. *Chemosphere* **2003**, *52*, 325–338. [[CrossRef](#)]
32. Von Glasow, R.; von Kuhlmann, R.; Lawrence, M.; Platt, U.; Crutzen, P. Impact of reactive bromine chemistry in the troposphere. *Atmos. Chem. Phys.* **2004**, *4*, 2481–2497. [[CrossRef](#)]
33. Oppenheimer, C.; Tsanev, V.I.; Braban, C.F.; Cox, R.A.; Adams, J.W.; Aiuppa, A.; Bobrowski, N.; Delmelle, P.; Barclay, J.; McGonigle, A.J. BrO formation in volcanic plumes. *Geochim. Cosmochim. Acta* **2006**, *70*, 2935–2941. [[CrossRef](#)]
34. Bobrowski, N.; Platt, U. SO₂/BrO ratios studied in five volcanic plumes. *J. Volcanol. Geotherm. Res.* **2007**, *166*, 147–160. [[CrossRef](#)]
35. Kern, C.; Sihler, H.; Vogel, L.; Rivera, C.; Herrera, M.; Platt, U. Halogen oxide measurements at Masaya Volcano, Nicaragua using active long path differential optical absorption spectroscopy. *Bull. Volcanol.* **2009**, *71*, 659–670. [[CrossRef](#)]
36. Boichu, M.; Oppenheimer, C.; Roberts, T.J.; Tsanev, V.; Kyle, P.R. On bromine, nitrogen oxides and ozone depletion in the tropospheric plume of Erebus volcano (Antarctica). *Atmos. Environ.* **2011**, *45*, 3856–3866. [[CrossRef](#)]
37. Kelly, P.J.; Kern, C.; Roberts, T.J.; Lopez, T.; Werner, C.; Aiuppa, A. Rapid chemical evolution of tropospheric volcanic emissions from Redoubt Volcano, Alaska, based on observations of ozone and halogen-containing gases. *J. Volcanol. Geotherm. Res.* **2013**, *259*, 317–333.
38. Theys, N.; van Roozendaal, M.; Dils, B.; Hendrick, F.; Hao, N.; de Maziere, M. First satellite detection of volcanic bromine monoxide emission after the Kasatochi eruption. *Geophys. Res. Lett.* **2009**, *36*, L03809. [[CrossRef](#)]
39. Hörmann, C.; Sihler, H.; Bobrowski, N.; Beirle, S.; Penning de Vries, M.; Platt, U.; Wagner, T. Systematic investigation of bromine monoxide in volcanic plumes from space by using the GOME-2 instrument. *Atmos. Chem. Phys.* **2013**, *13*, 4749–4781.
40. Bobrowski, N.; von Glasow, R.; Aiuppa, A.; Inguaggiato, S.; Louban, I.; Ibrahim, O.; Platt, U. Reactive halogen chemistry in volcanic plumes. *J. Geophys. Res. Atmos.* **2007**, *112*, D06311.
41. Roberts, T.; Martin, R.; Jourdain, L. Reactive bromine chemistry in Mount Etna’s volcanic plume: The influence of total Br, high-temperature processing, aerosol loading and plume–air mixing. *Atmos. Chem. Phys.* **2014**, *14*, 11201–11219. [[CrossRef](#)]
42. Galle, B.; Johansson, M.; Rivera, C.; Zhang, Y.; Kihlman, M.; Kern, C.; Lehmann, T.; Platt, U.; Arellano, S.; Hidalgo, S. Network for Observation of Volcanic and Atmospheric Change (NOVAC)—A global network for volcanic gas monitoring: Network layout and instrument description. *J. Geophys. Res. Atmos.* **2010**, *115*, D05304. [[CrossRef](#)]
43. Carn, S.A.; Krotkov, N.A.; Theys, N.; Li, C. Advances in UV Satellite Monitoring of Volcanic Emissions. In Proceedings of the 2021 IEEE International Geoscience and Remote Sensing Symposium IGARSS, Brussels, Belgium, 11–16 July 2021; pp. 973–976.
44. Taha, G.; Loughman, R.; Colarco, P.; Zhu, T.; Thomason, L.; Jaross, G. Tracking the 2022 Hunga Tonga-Hunga Ha’apai Aerosol Cloud in the Upper and Middle Stratosphere Using Space-Based Observations. *Geophys. Res. Lett.* **2022**, *49*, e2022GL100091. [[CrossRef](#)]
45. Carn, S.; Clarisse, L.; Prata, A.J. Multi-decadal satellite measurements of global volcanic degassing. *J. Volcanol. Geotherm. Res.* **2016**, *311*, 99–134. [[CrossRef](#)]
46. Platt, U.; Stutz, J. Physics of earth and space environments: Differential optical absorption spectroscopy: Principles and applications. *Phys. Earth Space Environ.* **2008**, 1–597. [[CrossRef](#)]
47. Qian, Y.; Luo, Y.; Si, F.; Yang, T.; Yang, D. Three-year observations of ozone columns over polar vortex edge area above West Antarctica. *Adv. Atmos. Sci.* **2021**, *38*, 1197–1208. [[CrossRef](#)]
48. Huang, Y.; Li, A.; Qin, M.; Hu, Z.; Xie, P.; Xu, J.; Duan, J.; Ren, H.; Tian, X.; Li, X. Nitrogen Oxides Spatial Distribution and Emissions with Mobile Multi-Axis Differential Optical Absorption Spectroscopy in Wuhan City. *Acta Opt. Sin.* **2021**, *41*, 1030002.
49. Qian, Y.; Luo, Y.; Si, F.; Zhou, H.; Yang, T.; Yang, D.; Xi, L. Total Ozone Columns from the Environmental Trace Gases Monitoring Instrument (EMI) Using the DOAS Method. *Remote Sens.* **2021**, *13*, 2098. [[CrossRef](#)]
50. Liu, W.Q. Opportunities and challenges for development of atmospheric environmental optics monitoring technique under “double carbon” goal. *Acta Opt. Sin.* **2022**, *42*, 0600001.
51. Yan, H. Volcanic SO₂ retrieved from GF-5 environmental trace gas monitoring instrument. *Natl. Remote Sens. Bull.* **2021**, *25*, 2326–2338.
52. Zhao, W.; Sun, C.; Guo, Z. Reawakening of Tonga volcano. *Innovation* **2022**, *3*, 100218. [[CrossRef](#)]
53. Lynett, P.; McCann, M.; Zhou, Z.; Renteria, W.; Borrero, J.; Greer, D.; Fa’anunu, O.; Bosserelle, C.; Jaffe, B.; la Selle, S. Diverse tsunamigenesis triggered by the Hunga Tonga-Hunga Ha’apai eruption. *Nature* **2022**, *609*, 728–733. [[CrossRef](#)]
54. Qian, Y.; Luo, Y.; Zhou, H.; Chang, Z.; Yang, T.; Xi, L.; Tang, F.; Si, F. Research on Retrieval of Sulfur Dioxide in Volcanic Region from EMI-2. *Acta Opt. Sin.* **2022**, *43*, 0601006.
55. Vandaele, A.C.; Hermans, C.; Fally, S. Fourier transform measurements of SO₂ absorption cross sections: II.: Temperature dependence in the 29 000–44 000 cm⁻¹ (227–345 nm) region. *J. Quant. Spectrosc. Radiat. Transf.* **2009**, *110*, 2115–2126. [[CrossRef](#)]

56. Bogumil, K.; Orphal, J.; Homann, T.; Voigt, S.; Spietz, P.; Fleischmann, O.C.; Vogel, A. Measurements of molecular absorption spectra with the SCIAMACHY pre-flight model: Instrument characterization and reference data for atmospheric remote-sensing in the 230–2380 nm region. *J. Photochem. Photobiol. A Chem.* **2003**, *157*, 167–184. [[CrossRef](#)]
57. Vandaele, A.C.; Hermans, C.; Simon, P.C.; van Roozendaal, M.; Guilmot, J.M.; Carleer, M.; Colin, R. Fourier transform measurement of NO₂ absorption cross-section in the visible range at room temperature. *J. Atmos. Chem.* **1996**, *25*, 289–305. [[CrossRef](#)]
58. Fleischmann, O.C.; Hartmann, M.; Burrows, J.P.; Orphal, J. New ultraviolet absorption cross-sections of BrO at atmospheric temperatures measured by time-windowing Fourier transform spectroscopy. *J. Photochem. Photobiol. A Chem.* **2004**, *168*, 117–132. [[CrossRef](#)]
59. Meller, R.; Moortgat, G.K. Temperature dependence of the absorption cross sections of formaldehyde between 223 and 323 K in the wavelength range 225–375 nm. *J. Geophys. Res. Atmos.* **2000**, *105*, 7089–7101. [[CrossRef](#)]
60. Hermans, C.; Vandaele, A.; Fally, S.; Carleer, M.; Colin, R.; Coquart, B.; Jenouvrier, A.; Merienne, M.-F. Absorption cross-section of the collision-induced bands of oxygen from the UV to the NIR. In *Weakly Interacting Molecular Pairs: Unconventional Absorbers of Radiation in the Atmosphere*; Springer: Dordrecht, The Netherlands, 2003; pp. 193–202.
61. Kleipool, Q.; Dobber, M.; de Haan, J.; Levelt, P. Earth surface reflectance climatology from 3 years of OMI data. *J. Geophys. Res. Atmos.* **2008**, *113*, D18308. [[CrossRef](#)]
62. Theys, N.; Campion, R.; Clarisse, L.; Brenot, H.; van Gent, J.; Dils, B.; Corradini, S.; Merucci, L.; Coheur, P.-F.; van Roozendaal, M. Volcanic SO₂ fluxes derived from satellite data: A survey using OMI, GOME-2, IASI and MODIS. *Atmos. Chem. Phys.* **2013**, *13*, 5945–5968. [[CrossRef](#)]
63. Carn, S.; Krotkov, N.; Fisher, B.; Li, C. Out of the blue: Volcanic SO₂ emissions during the 2021–2022 eruptions of Hunga Tonga—Hunga Ha’apai (Tonga). *Front. Earth Sci.* **2022**, *10*, 976962. [[CrossRef](#)]
64. Legras, B.; Duchamp, C.; Sellitto, P.; Podglajen, A.; Carboni, E.; Siddans, R.; Grooß, J.-U.; Khaykin, S.; Ploeger, F. The evolution and dynamics of the Hunga Tonga—Hunga Ha’apai sulfate aerosol plume in the stratosphere. *Atmos. Chem. Phys.* **2022**, *22*, 14957–14970. [[CrossRef](#)]
65. Menyailov, I. Prediction of eruptions using changes in composition of volcanic gases. *Bull. Volcanol.* **1975**, *39*, 112–125. [[CrossRef](#)]
66. Pennisi, M.; le Cloarec, M.F. Variations of Cl, F, and S in Mount Etna’s plume, Italy, between 1992 and 1995. *J. Geophys. Res. Solid Earth* **1998**, *103*, 5061–5066.
67. Allard, P.; Burton, M.; Muré, F. Spectroscopic evidence for a lava fountain driven by previously accumulated magmatic gas. *Nature* **2005**, *433*, 407–410. [[CrossRef](#)]
68. Aiuppa, A. Degassing of halogens from basaltic volcanism: Insights from volcanic gas observations. *Chem. Geol.* **2009**, *263*, 99–109. [[CrossRef](#)]
69. La Spina, A.; Burton, M.; Allard, P.; Alparone, S.; Muré, F. Open-path FTIR spectroscopy of magma degassing processes during eight lava fountains on Mount Etna. *Earth Planet. Sci. Lett.* **2015**, *413*, 123–134. [[CrossRef](#)]
70. Spilliaert, N.; Métrich, N.; Allard, P. S–Cl–F degassing pattern of water-rich alkali basalt: Modelling and relationship with eruption styles on Mount Etna volcano. *Earth Planet. Sci. Lett.* **2006**, *248*, 772–786.
71. Burton, M.; Allard, P.; Muré, F.; la Spina, A. Magmatic gas composition reveals the source depth of slug-driven Strombolian explosive activity. *Science* **2007**, *317*, 227–230.
72. Webster, J.; Sintoni, M.; de Vivo, B. The partitioning behavior of Cl, S, and H₂O in aqueous vapor–saline-liquid saturated phonolitic and trachytic melts at 200 MPa. *Chem. Geol.* **2009**, *263*, 19–36. [[CrossRef](#)]
73. Wennberg, P. Bromine explosion. *Nature* **1999**, *397*, 299–301. [[CrossRef](#)]
74. Von Glasow, R. Atmospheric chemistry in volcanic plumes. *Proc. Natl. Acad. Sci. USA* **2010**, *107*, 6594–6599. [[CrossRef](#)]
75. Bobrowski, N.; Giuffrida, G. Bromine monoxide/sulphur dioxide ratios in relation to volcanological observations at Mt. Etna 2006–2009. *Solid Earth* **2012**, *3*, 433–445. [[CrossRef](#)]
76. Lübcke, P.; Bobrowski, N.; Arellano, S.; Galle, B.; Garzón, G.; Vogel, L.; Platt, U. BrO/SO₂ molar ratios from scanning DOAS measurements in the NOVAC network. *Solid Earth* **2014**, *5*, 409–424. [[CrossRef](#)]
77. Cadoux, A.; Iacono-Marziano, G.; Scaillet, B.; Aiuppa, A.; Mather, T.A.; Pyle, D.M.; Deloule, E.; Gennaro, E.; Paonita, A. The role of melt composition on aqueous fluid vs. silicate melt partitioning of bromine in magmas. *Earth Planet. Sci. Lett.* **2018**, *498*, 450–463. [[CrossRef](#)]
78. Alletti, M.; Baker, D.R.; Scaillet, B.; Aiuppa, A.; Moretti, R.; Ottolini, L. Chlorine partitioning between a basaltic melt and H₂O–CO₂ fluids at Mount Etna. *Chem. Geol.* **2009**, *263*, 37–50. [[CrossRef](#)]
79. Zajacz, Z.; Candela, P.A.; Piccoli, P.M.; Sanchez-Valle, C. The partitioning of sulfur and chlorine between andesite melts and magmatic volatiles and the exchange coefficients of major cations. *Geochim. Cosmochim. Acta* **2012**, *89*, 81–101. [[CrossRef](#)]
80. Beermann, O.; Botcharnikov, R.; Nowak, M. Partitioning of sulfur and chlorine between aqueous fluid and basaltic melt at 1050° C, 100 and 200 MPa. *Chem. Geol.* **2015**, *418*, 132–157. [[CrossRef](#)]
81. Liu, Q. The Hunga Tonga–Hunga Ha’apai volcanic eruption and global climate change. *Ecol. Econ.* **2022**, *3*, 1–4. (In Chinese)
82. Guo, S.; Bluth, G.J.; Rose, W.I.; Watson, I.M.; Prata, A. Re-evaluation of SO₂ release of the 15 June 1991 Pinatubo eruption using ultraviolet and infrared satellite sensors. *Geochem. Geophys. Geosyst.* **2004**, *5*. [[CrossRef](#)]
83. Krueger, A.; Krotkov, N.; Carn, S. El Chichon: The genesis of volcanic sulfur dioxide monitoring from space. *J. Volcanol. Geotherm. Res.* **2008**, *175*, 408–414. [[CrossRef](#)]

84. Prata, A.; Folch, A.; Prata, A.; Biondi, R.; Brenot, H.; Cimarelli, C.; Corradini, S.; Lapierre, J.; Costa, A. Anak Krakatau triggers volcanic freezer in the upper troposphere. *Sci. Rep.* **2020**, *10*, 3584. [[CrossRef](#)] [[PubMed](#)]
85. Rose, W.I.; Delene, D.; Schneider, D.; Bluth, G.; Krueger, A.; Sprod, I.; McKee, C.; Davies, H.; Ernst, G.G. Ice in the 1994 Rabaul eruption cloud: Implications for volcano hazard and atmospheric effects. *Nature* **1995**, *375*, 477–479. [[CrossRef](#)]

Disclaimer/Publisher’s Note: The statements, opinions and data contained in all publications are solely those of the individual author(s) and contributor(s) and not of MDPI and/or the editor(s). MDPI and/or the editor(s) disclaim responsibility for any injury to people or property resulting from any ideas, methods, instructions or products referred to in the content.